Promotion of Instability of a Sinusoidally Deformed Flexible Plate and its Transition to Oscillatory Motions

Diego F. Muriel[1,2,*] and Edwin A. Cowen[1,†]

[1] *DeFrees Hydraulics Laboratory, School of Civil and Environmental Engineering, Cornell University, Ithaca, New York 14853, USA*

[2] *Laboratory for Experimental Fluid Dynamics, Department of Mechanical Engineering, Johns Hopkins University, Baltimore, Maryland 21218, USA*

(Received 20 October 2019; published 27 January 2020)

We experimentally study the transition to large oscillatory motions of a thin elastic plate buckled into a second mode sinusoidal deformation. This deformation, intended to promote the onset of structural instabilities, is created by applying a permanent external net compressive force to the plate through a series of equispaced tension lines. These lines are attached to the two lateral edges of the plate, which are oriented parallel to the mean flow direction. We subject the deformed plate to an incompressible flow and find an early onset of the flutter instability (lower critical flow velocity, U_c) and increased range of periodic large oscillatory motions relative to previous studies of plates mounted in flag or inverted-flag configurations. No upstream vortex shedding or additional transversal rigidity is provided to achieve this lower U_c, which are methods used by previous researchers to initiate instability. The reduced U_c is instead achieved by the combination of three mechanisms: a deformed plate that exhibits bistability, the destabilizing action of the net compressive force on the plate, and the pressure drag on the plate existent prior to large plate oscillations. Subjected to a mean flow, U_o, the deformed plate evinces three states of motion: (a) a buckled plate with small perturbations for $U_o < U_c$ (perturbations are of the order of 0.1% of the plate's length); (b) a plate with large oscillatory motions appearing as the superposition of traveling and standing waves for $U_o > U_c$, showing fundamental oscillatory frequencies f_o, which scale with U_o, along with higher harmonics; and (c) a plate with chaotic oscillatory motions for $U_o > U_t$, a transitional flow velocity where $U_t > U_c$, characterized by a broad frequency spectrum still with a characteristic f_o, and slightly reduced relationship between U_o and f_o.

DOI: 10.1103/PhysRevApplied.13.014050

I. INTRODUCTION

Plates and membranes interacting with fluid flows are canonical problems exhibiting a broad range of physics concerning the onset of flutter instabilities. Such instabilities, which at one time were considered failure states, are now exploited for novel applications such as adaptive flow control [1,2], energy harvesting [3–10], and projectile stabilization [11,12]. Progress understanding the physics of these instabilities has been broadly useful, explaining different phenomena such as biological flows [13–18], animal locomotion [19–22], and induced vibrations in structures [23–26]. In general, the interaction of rigid or flexible plates with a flow is a problem described by the interaction between the elastic, inertial, and damping forces of the structure and the hydrodynamic forces of the fluid flow [27,28].

Efforts have been made to leverage these instabilities in the area of energy harvesting, where the basic concept is to harness the energy of the instability induced within the plates, for example, by ambient vibrations [29] or fluid forcing [3–10]. In general, conversion efficiency is paramount. When exploiting ambient vibrations, buckled configurations of plates have been used to extend the energy harvesting potential to a broader range of forcing frequencies [30–32]. In a similar manner, when exploiting fluid forcing, different geometrical configurations have been implemented to increase operational range (defined as the range of flow velocities where stable oscillations of the plate occur) and reduce the critical flow velocity, U_c, at which the flutter instability initiates [4,6–8,33–35]. Historically, Euler buckling was the first example of elastic bifurcation and instability. It involves the spontaneous breaking of symmetry at loads that exceed a critical compressive load [36]. Conversely, flapping is a dynamic instability, which can be triggered by either flutter or divergence instabilities. The former is an oscillatory vibration

*dfm99@cornell.edu
†eac20@cornell.edu

of increasing amplitude and the latter is an exponentially growing motion. Buckling occurs through divergence. A detailed treatment of instabilities is presented by Bigoni [37], whereas the behavior of rigid and flexible structures under fluid forcing, the governing equations, and the nature of the instabilities are thoroughly covered by Dowell [38, 39], Shelley and Zhang [28], Dowell and Ilgamov [40], and Paidoussis [41,42]. Here, elastic buckling instabilities are not to be confused with purely elastic instabilities occurring in viscoelastic fluids at Weissenberg numbers, Wi, of order unity and vanishingly small Reynolds numbers, Re [43].

An extensive literature on the onset of instability in plates mounted in flag or inverted-flag configurations can be found in Tang and Paidoussis [44], Eloy *et al.* [45,46], Michelin *et al.* [47], Alben and Shelley [48], Doaré *et al.* [49], Eloy *et al.* [50], Schouveiler and Eloy [51], and Fan *et al.* [52]. These works summarize and group different theoretical and numerical efforts and identify the key aspects leading to the onset of the instability. Specifically, they explore the critical velocity for the onset of the instability, the presence and breadth of the hysteresis loop on the critical velocity, confinement effects, and aspect ratio effects, amongst others. Further details on experimental and numerical studies can be grouped in the following nonexhaustive areas: the fluid-structure coupled behavior excited or forced by vortex shedding from an upstream (relative to the plate) structure [4,6,7]; the efficiency of energy extraction [5,9,10]; alternative configurations to decrease U_c [8,34,35]; the coupling in a fluid-solid-electric configuration [53–58]; periodically pitching and heaving rigid foils exploiting vortex separation [59–69]; and rigid cylinders under vortex-induced vibrations [70,71].

In terms of energy harvesting efficiency and regardless of the energy harvesting approach—the use of a mechanical coupling with an external generator [3] or the use of piezoelectric materials [72]—the fundamental goal is to achieve stable structural oscillatory motions at as low a flow velocity (i.e., as low a U_c) as possible [33,58]. For example, piezoelectric flags (canonical configuration, that is, a flexible plate tethered at its leading edge) are known to exhibit high U_c and require even higher flow velocities for consistent oscillations [4,6,33]. In addition, three-dimensional effects are known to delay the onset of instability in flag configurations [50,73]. Furthermore, alternative configurations, such as the inverted flag (i.e., a flexible plate tethered at its trailing edge), achieve oscillatory motions at lower U_c relative to the canonical configuration [33], however, at a limited operational range.

A. Our study

We investigate the interaction of a sinusoidally deformed flexible plate with a uniform turbulent incompressible mean flow (with bulk velocity U_o) and study its behavior in the presence of the plate's large oscillatory motions ($U_o > U_c$) as well as the absence of such motion ($U_o < U_c$). We demonstrate that a plate's elastic instability (buckled configuration) can be used to lower the critical flow velocity, U_c, at which flapping initiates, while simultaneously preserving or increasing its operational range. Specifically, we confirm that the sinusoidally

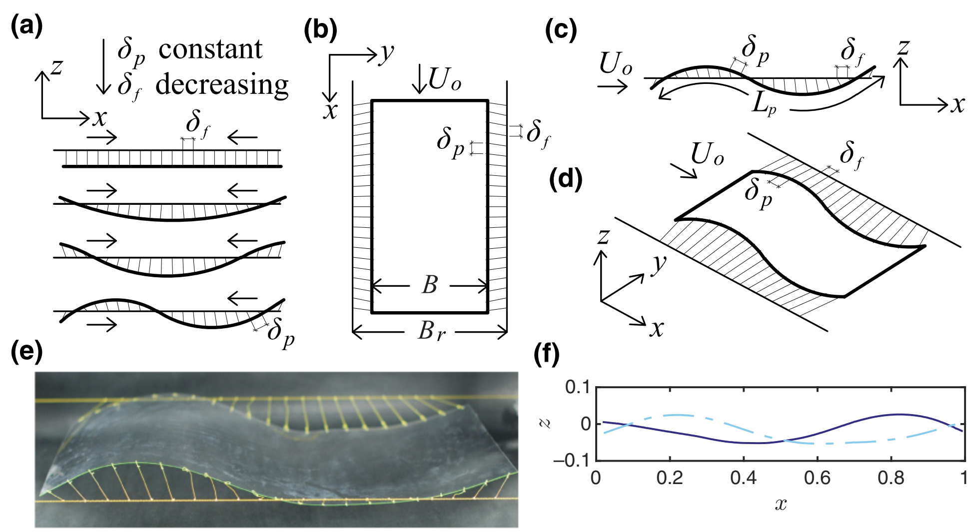

FIG. 1. Isometric representation of the deformed plate (panels (a) to (d) are adapted from Muriel *et al.* [74]). (a) Realization of sinusoidal deformation: effect of decreasing separation distance between tension line attachment points on side frame lines, δ_f, relative to a constant separation distance between tension line attachment points on the plate, δ_p, where in the topmost figure $\delta_f = \delta_p$. (b) Top view: flow velocity upstream of the prototype, U_o, plate's width, B, separation between side-frame lines, B_r. (c) Side view: plate's length, L_p. (d) Isometric projection. (e) Experimental realization of a second mode deformation. (f) Plot depicting two locally stable deformations ($x = X/L_p$ and $z = Z/L_p$).

buckled plate shown in Fig. 1 demonstrates a lower U_c and broader operational range than those found for flag or inverted-flag configurations with no need for vortex shedding from an upstream structure, a common tactic in flag- and inverted-flag-type configurations to lower U_c. The buckled configuration yields consistent oscillations at low flow velocities, allows the use of materials with higher damping modulus, and produces consistent oscillatory events at higher flow velocities, therefore achieving a broader operational range.

Herein, we present evidence of three mechanisms contributing to the onset of large oscillatory motions at low U_c: (1) the bistability of the buckled plate induced by net external compression, which forces the device into a state of permanent deformation and local equilibrium; (2) the destabilizing action of the net compressive force on the plate; and (3) the resultant unsteady flow field over the plate that induces pressure drag and lift prior to the onset of large-amplitude oscillatory motions. Moreover, we show that the deformed plate can be characterized under three states of motion: (a) a buckled plate with small perturbations at $U_o < U_c$ (perturbations of the order of 0.1% of the plate's length); (b) a plate with large oscillatory motions appearing as a superposition of traveling and standing waves for $U_o > U_c$, showing fundamental oscillatory frequencies f_o, which scale with U_o, along with higher harmonics; and (c) a plate with chaotic oscillatory motions for $U_o > U_t$, a transitional flow velocity, characterized by a broad frequency spectrum still with a characteristic f_o, and slightly reduced relationship between U_o and f_o.

II. METHODS

A. A buckled flexible plate

The plate is buckled into a sinusoidal shape by the action of equispaced tension lines [Fig. 1(a)]. We start from a flat planar state [Fig. 1(a), top] and increase the net compression force to our plate by decreasing the attachment point separation distance on the frame, δ_f. When this net compression exceeds Euler's critical load, large deflections appear, first, as a mode 1 deformation and, then, as a mode 2 deformation [Fig. 1(a), bottom]. A mathematical model of the described deformation is presented by Muriel and Cowen [75].

The plate is made of a single translucent polycarbonate sheet with thickness $\delta = 0.400$ mm, length $L_p = 60$ cm, width $B = 30$ cm, density $\rho_p = 1.14$ g/cm^3, water absorption 0.15%–0.34%, and tensile modulus $E = 1.97$ GPa. The applied net compression force is created using inner tension lines mounted to parallel side-frame lines. The side-frame lines are made of a 0.4 mm diameter microfilament braided line (Spectra®) rated to 471 N. Similarly, the tension lines are composed of a microfilament with length $L_s = 7.6$ cm, separation distance along the plate of $\delta_p = 2.90$ cm and separation distance along the side frame of $\delta_f = 2.45$ cm. This difference between the two separation distances (δ_p and δ_f) provides the external compression force necessary to induce the plate's deformation, with maximum achievable deformation height of 28.9 mm ($\sim 0.05 L_p$, crest to trough). The entire device is mounted within a frame made of extruded aluminum alloy, which sets the separation between side-frame lines to $B_r = 44.10$ cm, and positions the plate 15.0 cm above the bottom of a recirculating-type open-channel flume.

B. Nondimensional parameters

We define

$$\mathrm{Re} = \rho_f U_o L_p/\mu, \tag{1a}$$

$$u_o = U_o\sqrt{\rho_f B L_p^3/D}, \tag{1b}$$

$$r = \rho_p \delta/\rho_f L_p, \tag{1c}$$

$$m_a = M_a/\rho_f L_p, \tag{1d}$$

$$\beta = D/\rho_f U_o^2 L_P^3, \tag{1e}$$

$$\text{and } p^* = P/\rho_f U_o^2 L_P, \tag{1f}$$

where Eq. (1a) is the Reynolds' number based on the length of the plate, Eq. (1b) is the reduced velocity, Eq. (1c) is the dimensionless mass ratio, Eq. (1d) is the dimensionless added mass, Eq. (1e) is the dimensionless bending stiffness, and Eq. (1f) is the dimensionless compression force. Here, ρ_f represents the density of the fluid, U_o the upstream bulk velocity, μ the dynamic viscosity of the fluid, D the flexural rigidity defined as $D = EI/(1-\nu^2)$, with E being the Young's modulus, I the area moment of inertia, and ν Poisson's ratio [76], M_a the dimensional added mass, and P the dimensional compression force.

We maintain material and geometric properties across all experiments and vary u_o and Re from 9.2 and 4.1×10^4 up to 82.2 and 3.7×10^5, respectively. Here r is equal to 7.6×10^{-4}, β varies from 3.6×10^{-3} to 4.4×10^{-5} from lowest to highest flow velocity with fixed D, and p^* varies from 4.4×10^{-1} to 5.4×10^{-3} from lowest to highest flow velocity with fixed P. The dimensionless form of the critical (u_c), bulk (u_o), and transitional (u_t) velocities will be used from now on. Note that the specific u_o where oscillatory motions first occur is by definition u_c.

C. Experimental facility

Experiments are conducted in an 8.0 m long, 0.60 m wide recirculating-type open-channel flume with glass sidewalls and super abrasion resistant (SAR) acrylic bed in the DeFrees Hydraulics Laboratory in the School of Civil and Environmental Engineering at Cornell University. Two variable frequency controlled centrifugal pumps drive a constant water depth across all experiments of $h =$

37.0 cm [$h = 35.0$ cm for particle image velocimetry (PIV) measurements]. The bed slope is set at 0.0 (i.e., horizontal), with negligible streamwise acceleration [$\partial U_b^2/\partial x \sim 0$ to experimental uncertainty, with the depth-averaged mean velocity at the centerline of the flume defined as $U_b \equiv (1/h)\int_0^h U(z)\,dz$]. A turbulent boundary layer is tripped by a 4 mm tall rectangular steel bar mounted on the bed in the transverse direction and located at the entrance of the flume test section, downstream of inlet conditioning screens. A 15 μm porous felt is used to filter suspended particles of diameter greater than that of the felt. The coordinate system is defined with x in the streamwise direction, z as the vertical distance from the bed to the water surface (positive upwards), and the y direction is set by the right-hand rule.

D. Experimental study cases and techniques

Three distinct datasets are collected. First, acoustic Doppler velocimetry (ADV; Nortek Vectrino equipped with + firmware) measurements are used to determine the onset of large oscillatory motions and to characterize the evolution of the plate's oscillatory frequency, f_o, as a function of u_o. Second, imaged-based edge detection is used to characterize the plate's large oscillatory motions, including their wave composition and frequency, again as a function of u_o. Third, PIV measurements are made, which are then used to calculate the pressure fields and forces acting on the plate. To obtain time-averaged pressure fields, we assume the time-averaged flow field to be two dimensional and integrate the Reynolds-averaged momentum equation [77,78]. A detailed summary of the study cases using ADV, image-based point detection, image-based edge detection, and PIV can be found in Appendix A. Details on uncertainty analysis can be found in Appendix B.

1. Particle image velocimetry

The flow velocity in the vicinity of the model is measured with PIV. Digital images are collected with two Andor Zyla 5.5 MP sCMOS cameras (2160 × 2560 pixels, 16 bits per pixel, run at 20 frames per second, yielding 10 Hz velocity fields) equipped with 50 mm Nikkor lenses. The image area is illuminated with a Spectra Physics PIV 200-10 Nd:YAG laser (200 mJ/pulse at 532 nm, 10 Hz dual head). A laser light sheet is formed using a cylindrical lens ($f = -6.4$ mm) and the beam is focused with one spherical lens ($f = 1500$ mm) to provide a maximum light sheet thickness of 1 mm over the field of view. This configuration provides a resolution of 144 μm/pixel covering an area of 31.1 cm × 73.7 cm. Upstream bulk velocity is measured with a single ADV with its measurement volume located $5L_p$ upstream from the leading edge of the plate and 15.0 cm above the bed (i.e., at the mean elevation of the plate), with a sampling frequency of $f_s = 200$ Hz.

A Berkeley Nucleonics Inc. (San Rafael, Calif.) BNC500A digital delay generator is used to trigger the flash lamps and Q switches on the Nd:YAG laser system with temporal delay between image pair illuminations, Δt, chosen to limit the maximum particle motion within an image pair to ~10 pixels, allowing a final PIV subwindow of 32 × 32 pixels to be used to determine the displacement field. The flume is filled with water to the desired depth and seeded with Sphericel particles (hollow glass spheres, mean density 1.1 g/ml, median diameter 11.7 μm, manufactured by Potters Industries, Inc., Valley Forge, Pa.).

Prior to cross-correlation analysis, an intensity-count-based digital mask is used to reduce the influence of the highly reflective plate. We do not conduct a correlation-tracking-based mask technique [79]; instead, after the mean velocity field is subtracted from each image, pixels inside the digital mask are set to zero.

Image pairs in the x–z plane are analyzed with the dynamic subwindow PIV scheme described by Cowen and Monismith [80] and extended to second-order accurate based on Wereley and Meinhart [81]. A total of 4250 image pairs at 5 Hz are analyzed for cases at $u_o < u_c$. The analysis comprises an iterative scheme with 5 displacement estimate passes, with the final pass utilizing 50% overlapped 32 × 32 pixel subwindows, yielding a grid resolution of approximately 2.3 mm vertically and horizontally, resulting typically in 20 724 analyzed subwindows per image pair. The full field of view is composed of two of these independent data fields (i.e., two cameras, each recording half of the field of view), forming a grid of 132 × 314 vectors in the vertical and horizontal axes, respectively.

III. RESULTS AND ANALYSIS

A. The transition to large oscillatory motions

Our results show that large structural oscillations are initiated at $u_c = 25.7$ (Fig. 2). The limits of the hysteresis loop, where u_c differs if it is found by decreasing or increasing u_o, are small and are determined to be $\pm 0.02u_c$. We test this same plate (i.e., material, thickness, and aspect ratio), in a flag configuration, that is, with only a tethered leading edge. This test yields weak perturbations up to $u_o = 28.1$ (amplitude of the perturbations are smaller than the order of 0.1% of the plate's length), small amplitude and intermittent oscillatory motions up to $u_o = 61.2$ (hovering), and shows no evidence of a developed flutter instability up to $u_o = 94.5$, where our facility reaches its maximum u_o. The observed perturbations at these velocity ranges for our flag type configuration tests are attributed to surface and three-dimensional effects (see Supplemental Material for video *VFlagType.mp4* of the tethered leading edge configuration at $u_o = 94.5$ [82]).

As a comparison, Shelley *et al.* [83] studied a flag-type configuration that remained flat even at speeds as

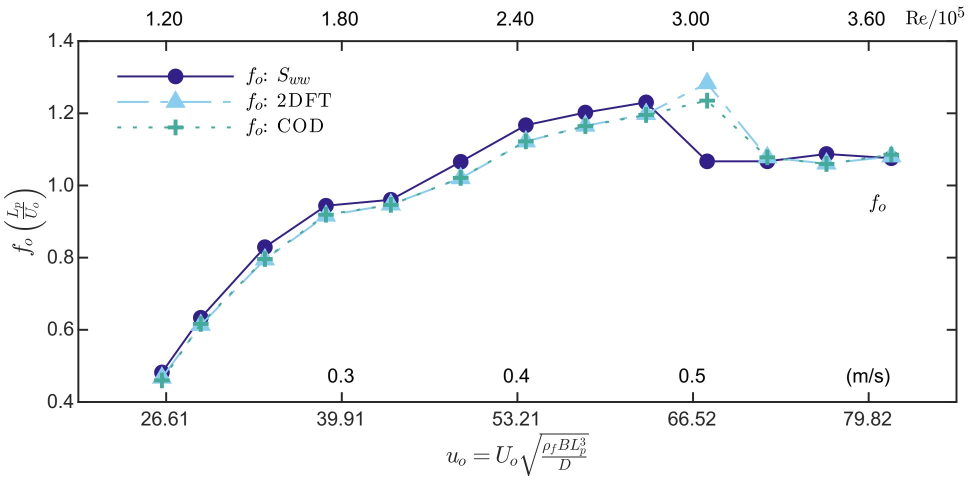

FIG. 2. (a) Evolution of oscillatory frequency, f_o, as a function of flow velocity, u_o. Results are for f_o through spectral analysis of velocity measurements of a fluid parcel, S_{ww}, and through two-dimensional Fourier transform (2DFT) and complex orthogonal decomposition (COD) of the plate's image-based-detected edge.

high as $U_o = 0.90$ m/s, which can be rendered dimensionless using their material properties, corresponding to $u_o = 4.2 \times 10^4$. As they discussed, the absence of instability at such a high flow velocity is due to the inability of the flag's inertial forces to overcome the fluid's stabilizing forces (drag). In an effort to incite instability, Shelley *et al.* [83] used copper strips to add lateral stiffness and achieved transition to a flapping state at $U_c = 0.81$ m/s ($u_c = 197.0$). Three-dimensional effects at $u_o < u_c$ are prevented in our study by the action of the tension lines, which do not add inertia to the system. An additional study on heavy flags reported a critical velocity of $U_c = 0.57$ m/s [9], which in dimensionless form is $u_c = 76.2$. Additional stiffness to this system is provided by ionic copolymers attached to the surface of a flexible mylar sheet, resulting in a lower u_c than that of Shelley *et al.* [83].

Care must be taken when exploring such differences in u_c for different configurations. For example, in the presence of a buckled plate (i.e., this study), an unsteady flow field is present before oscillations start. In contrast, on a flat plate the evolution of oscillatory motions is coupled to the evolution of the unsteady hydrodynamic forces. We therefore demonstrate an alternative configuration to achieve the transition of a flexible plate to a flapping state, where a dominant pressure drag overcomes the stabilizing forces of the system, therefore reducing u_c compared with that expected for flag-type configurations. In the following sections we present the main mechanisms for this reduction.

B. Mechanism one: bistable systems

A system that exhibits two stable equilibrium states, known as a bistable system, can be described by a unique double-well restoring force potential [29]. Through stable state switching, these systems transition from one stable state to the other, causing large-amplitude motion. It has been demonstrated that bistable energy harvesters are an improvement upon their linear counterparts operating in their steady-state vibrational environments. In addition, they have been analytically and experimentally shown to provide as much as an order of magnitude more harvested energy [29–32,84].

To achieve a bistable system and reduce the requisite dynamic external loading (i.e., fluid forcing) necessary to induce large oscillatory motions on our plate, we provide a net external compressive force and create the well-known buckling instability. The second mode deformation, seen in Fig. 1(e), is stabilized through the action of external constraints (i.e., tension lines). Our plate, which by design is free to move, provides no opportunity to apply moments or internal forces at the boundaries. Therefore, the plate requires the action of the tension lines to stabilize the sinusoidal deformation and create the bistable system.

The solution to the nonlinear system of equations describing the plate's shape shows more than one possible structural deformation for a single external compressive force [see Figs. 1(d)–1(f), and Muriel and Cowen [75]]. This is evidence of the instability (i.e., buckling) and corroborates the formation of a bistable system. More importantly, the action of any additional external force, either numerically or experimentally, will induce intrawell oscillatory motions or large motions, to be described in the following sections.

C. Mechanism two: external compression

It has been demonstrated by Dowell that the flutter-type instability is aggravated by a compressive in-plane load for double-pinned plates [85–88] and for double-pinned cylinders by Paidoussis [89]. Following Connell and Yue [90], a flat plate under compression is described by

$$(r + m_a)\frac{\partial^2 z}{\partial t^2} + \left(p^* - 1.3\mathrm{Re}^{-1/2} + m_a\right)\frac{\partial^2 z}{\partial x^2} + \beta\frac{\partial^4 z}{\partial x^4} + 2m_a\frac{\partial^2 z}{\partial x \partial t} = 0, \quad (2)$$